Excerpt from the Proceedings of the 2011 COMSOL Conference in Stuttgart

Influence of Vickers Indenter Tip Geometry on the Macro-indentation Properties of γ-TiAl Alloys

R. Cagliero, and G.Maizza*
Dipartimento di Scienza dei Materiali ed Ingegneria Chimica, Politecnico di Torino
*Corresponding author: C.so Duca degli Abruzzi 24, 10129, Torino, Italy, maizza@polito.it

Abstract:
The instrumented indentation testing of γ-TiAl imposes the use of large loads only possible with diamond pyramidal indenters. The geometry of such indenters (e.g. Vickers indenter) has to be precisely defined. In addition, the so-called zero-point of the loading curve (i.e. the first point of the indenter coming into contact with the sample) has to be precisely located to ensure accurate measurements. Computer models may help to appropriately post-process the raw data by taking into account several crucial factors, among these, the initial stage of the loading curve, the influence of the actual indenter tip geometry, friction effects and pile-up or sink-in phenomena if any.
In this work the influence of the geometry of the indenter tip on relevant indentation properties is investigated during experimental and numerical macro-instrumented indentation in the case of a hip-homogenized γ-TiAl alloy. The employed macro-instrumented indentation is characterized by loading forces ranging from 2 to 200 N. The developed 3D structural contact model is implemented in the Comsol Multiphysics 3.5a environment and involves large displacements, strong singularity and materials non linearity.

Keywords: Vickers hardness, titanium aluminide, depth sensing indentation, elasto-plastic, contact mechanics, friction.

1. Introduction

The present work focuses on the macro-scale indentation behavior of bulk γ-TiAl based alloys (Ti-48Al-2Cr-2Nb) by experimental and modeling means.
In the late 1970s intermetallic alloys emerged as new structural materials for high temperature applications in the aerospace and the automotive industry [1,2]. TiAl based alloys have excellent mechanical specific properties, together with creep and oxidation resistance. However, they are penalized by very low ductility at room temperature. These peculiar properties are due to the presence in the alloy of at least 12%$_w$ of γ-TiAl, an ordered intermetallic compound consisting in a slightly tetragonal cell of alternating planes of Ti and Al atoms [3,4]. Electron beam melting (EBM) is a vacuum based advanced manufacturing method which employs a focused electron beam to additively sinter/melt pre-alloyed γ-TiAl powders and to subsequently build layer by layer the desired near-net shape product with the aid of a CAD system. However due to relatively long processing time, the final product may be subject to excessive oxygen enrichment and/or aluminum evaporation. Either effects may induce dramatic brittleness in the final product. In fact, due to vacuum leaks oxygen can be infiltrated in the EBM chamber and Al may escape from the processed powders owing to the high temperatures originated by the electron beam. Hence the need of a viable method is demanded to effectively set up the manufacturing process and to rapidly assess the mechanical properties without resorting to expensive and time-consuming chemical analysis.
Instrumented indentation (also known as depth sensing indentation) is a non-destructive test method typically used to estimate the mechanical properties of small volumes of materials. This test employs high resolution instrumentation to continuously record both the loads and the displacements of an indenter during a controlled loading-holding-unloading cycle. The resulting indentation curve is then commonly analyzed by the Oliver and Pharr method.
From indentation curves both elastic and plastic mechanical properties can be derived. Among them, indentation hardness and indentation modulus are becoming very important design parameters. As γ-TiAl-based alloys are sufficiently hard, they require high forces when inspected by depth sensing indentation. Under these conditions pyramidal indenters made of diamond (like Vickers or Berkovich indenter) are suited. However, accurate indentation results can be gained only if the geometry of the indenter is

well defined and if the zero-point (i.e. the first contact point) is precisely located. In fact, due to the intrinsic crystallographic structure of diamond, a real Vickers indenter is characterized by an offset near to the tip that can affect the value of the contact area and, in turn, the final hardness measurements. Moreover, a tip roundness can be recorded in the case of worn or dusty indenter and even small variations in the apex angle may lead to non-negligible errors in the indentation curves. The accuracy in the determination of the zero point is also function of the geometry of the indenter. Especially in the macro-range, the mis-location of the zero-point may lead to an erroneous translation of the indentation curves.

The use of an aiding finite element model, embodying friction effects and capable of resolving pile-up/sink-in phenomena (figure 1) can permit to simulate realistic indenter tips and, thus, to accurately predict the initial stage of the loading curve.

Macro-indentation experiments are here executed using a specially developed prototype indentation machine. The macro range has been chosen in order to promote a massive mechanical response from the testing material.

Figure 1. Sink-in and pile-up phenomena [5].

2. Vickers instrumented indentation

Hardness is commonly defined as the resistance to plastic deformation of a material. Traditional hardness tests directly measure the residual imprint originated by pressing the indenter over the material with a definite force (typically ranging from 0.1 to 980.7 N) [6] and then evaluates the hardness value by means of the ratio between the force and the sloping area of the indenter (which is assumed to be a perfect pyramid):

$$HV = 0.102\frac{2F\sin\frac{136°}{2}}{d^2} \approx 0.1891\frac{F}{d^2}$$

where F is the test force in N and d is the average in mm of the two diagonal lengths taken from the residual imprint. The latter is evaluated by means of an optical microscope.

Both traditional hardness and depth sensing indentation can make use of Vickers indenters. These indenters are made of diamond and have the form of a squared right pyramid with an apex angle of 136°.

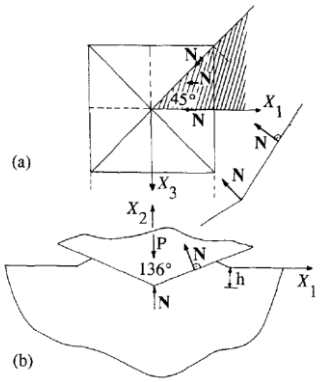

Figure 2. Ideal geometry of Vickers indenter [5].

As loads and displacements are continuously recorded during instrumented indentation, an indentation curve (IC) can be acquired. The post-processing procedure of the ICs may follow that proposed by Oliver and Pharr method which requires the evaluation of a number characteristic depths of penetration [7].

A unique advantage of indentation properties compared to traditional hardness is that the measurement of the sloping area (by means of an optical microscope) is not required rather a contact area is defined as a projected area and evaluated using the Sneddon's formula.

This formula helps calculate the deflection of the sample surface and hence the required contact depth. For Vickers indenter, the contact area is [8,9,10]:

$$A_c = 24.50h_c^2$$

where the contact depth h_c is estimated as:

$$h_c = h_{\max} - \zeta\frac{P_{\max}}{S}$$

where $\zeta = 0.75$ for a Vickers indenter.

a)

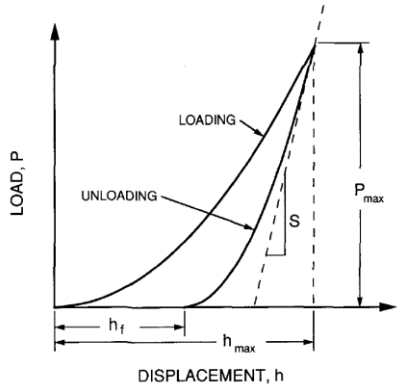

b)

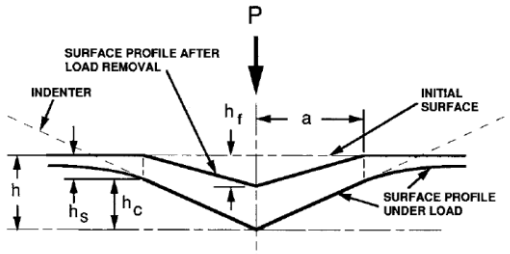

Figure 3. a) Typical indentation curve for an elastoplastic material (h_e = depth elastically recovered, h_p = final depth of the residual imprint, h_{max} = maximum depth of penetration, P_{max} = maximum force, S = initial unloading stiffness); b) other characteristic penetration depths (h_s = displacement of the surface at the contact perimeter, h_c = contact depth) [7].

2.2 The geometry model

The proposed 3D Vickers hardness model is based on a stress-strain analysis taking into account only a quarter of the whole geometry (see Fig.4).

The base of the indenters is always modeled by an isosceles triangle with angles of 45° and sides of 0.884 mm and 1.250 mm.

An additional region of height of 0.884 mm is always added to the pyramidal tip in order to reach a mechanical equilibrium between the two contact bodies consisting of the sample disk and the indenter.

The radius and thickness of the sample disk are 1.5 and 0.9 mm respectively.

In this work, different indenter tip geometries are considered in order to evaluate their influence of on the resulting ICs.

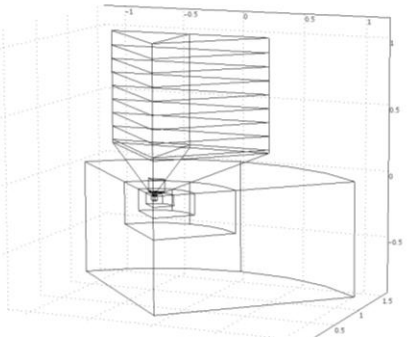

Figure 4. 3D model geometry of Vickers indentation.

Initially, an ideal Vickers tip is used to validate the geometry model and to calculate the ideal indentation curve. Specifically, the calculated indentation curve is compared with experimental measurements using a non severely worn Vickers indenter. These results are then compared to those obtained by a truncated Vickers tip and by a blunted Vickers tip. The former geometry is used to take into account the offset effect due to the crystallographic structure of the diamond. The latter indenter represents a typical worn or a dusty indenter having also slightly changed apex angles.

The ideal Vickers indenter has been modeled by means of a right pyramid with an apex angle of 136° and a base composed of an isosceles triangle, angles of 45° and sides of 0.884 mm and 1.250 mm. For sake of completeness, an ideal pyramidal indenter tip with apex angles of 136.4° is also modeled.

The tip of the truncated indenter is inspire by an ideal Vickers tip having apex truncated at an height of 0.0125 mm. Essentially, a volume of 0.003248 mm^3 has been removed from the ideal indenter. This means that there exist an initial contact triangular surface between the indenter and the sample characterized by a very small area of 0.0009572 mm^2.

On the other hand, the so-called blunted Vickers indenter is modeled starting from an ideal Vickers tip after truncation at a height of 0.00875 mm and blunting it with a 5° tilted plane to remove almost the same volume of material, i.e.

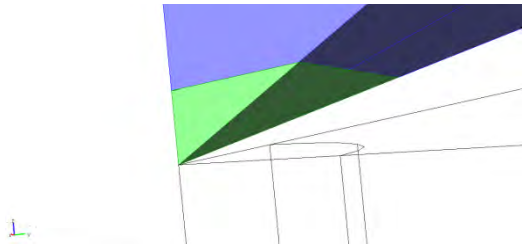

Figure 5. Comparison between the ideal Vickers tip (green) and the truncated Vickers tip (blue).

0.003246 mm^3, to allow a comparison with the truncated Vickers indenter. The initial contact surface consists of a smaller triangular area of 0.0000877 mm^2. The tilted plane implies that a non ideal sloping area of 0.0006858 mm^2 has to be surmounted before reaching the contact between the ideal Vickers boundaries and the sample. Blunted indenters with apex angles of 135° and 141.3° are also considered. To reduce the effect of the non ideal sloping boundary areas, a so-called slightly blunted Vickers indenter, being truncated at a height of 0.003825 mm and blunted by a 5° tilted plane, is also considered. In this case, the removed volume is reduced by the 75% with respect to the blunted indenter.

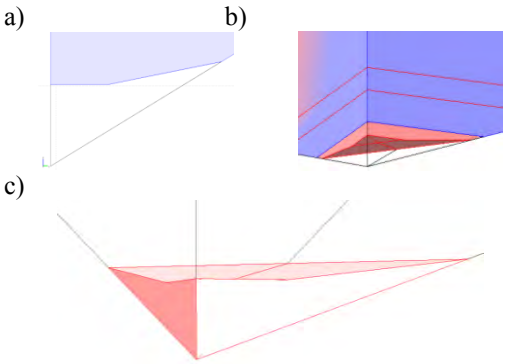

Figure 6. a) y-z plane: comparison between the ideal tip and the truncated tip (blue); b) 3D view: comparison between the ideal tip, the truncated tip (blue) and the blunted tip (red); c) 3D view: volume removed from the ideal tip in order to model the blunted tip.

2.2 The bulk elastoplastic model and the contact model

The sample disk is considered to behave elastoplastically while undergoing isotropic hardening [11,12,13,14]:

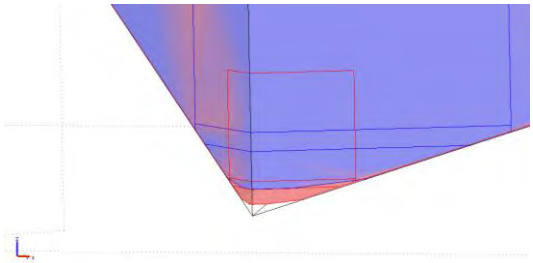

Figure 7. Comparison between the blunted tip (blue), the slightly blunted tip (red) and the ideal Vickers tip.

$$\sigma_{yhard} = \sigma_{\exp}(\varepsilon_{eff}) - \sigma_y \qquad (1)$$

where σ_y is yield stress and σ_{exp} is a true stress-true strain tensile curve modeled by the Young's modulus, the yield stress and the isotropic tangent modulus derived by an experimental tensile test. The total effective strain ε_{eff} across the disk is the sum of the plastic strain ε_{pe} and the elastic strain ε_e:

$$\varepsilon_{eff} = \varepsilon_{pe} + \frac{\sigma_e}{E}$$

where σ_e is the von Mises effective stress.
The indenter is assumed to behave isotropically.

2.1 Boundary conditions

The imposed boundary conditions are as follows:

b.1 symmetry plane condition at boundaries along the symmetric plane
b.2 fixed constraint at the bottom of the sample disk
b.3 kinematic constraint along the z-direction
b.4 all other boundaries are considered free.

Only in the case of the truncated indenter, the pyramid has an additional constraint along the x- and y-axis in order to control the deformation of the faces of the indenter.
The b.3 boundary condition is specified at the top of the indenter using a user's defined displacement parameter. This parameter will be important to control the displacement of the indenter with respect to the disk.

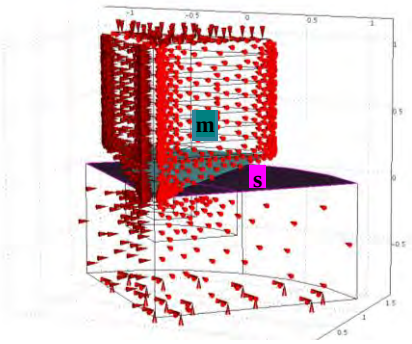

Figure 8. Boundary conditions and contact pair (m = master, s = slave).

2.5 The discretization mesh

Domain discretization is a critical step in finite element calculations, especially when dealing with contact mechanics, since during indentation, large displacements may occur thereby involving compenetration regions and/or voids which may cause stopping of the model calculation.
The sample disk is divided into five sub-domains (figure 4) to enable selective refinement at the beginning and during the calculation based on the local nature of the contact. Specifically, for the smaller domain initially involved in the contact, the maximum triangular element size is set to 0.021 mm. For the other four domains, a maximum element size of 0.031, 0.096, 0.280 and 0.840 mm is set respectively.

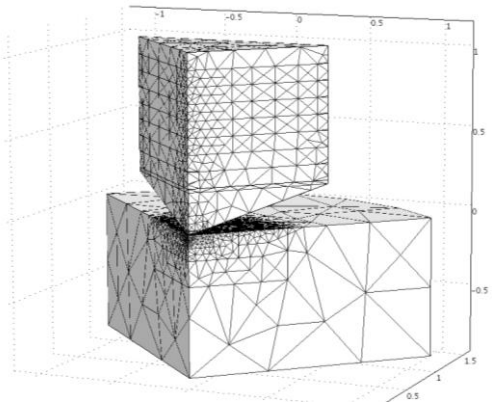

Figure 9. Initial mesh.
To overcome the ideally infinite pressure problem in the case of the ideal tip a coarse mesh is imposed at the initial contact point for the first value of displacement parameter (Step I). After reaching a good starting solution, the mesh is progressively made denser in critical regions to increase the accuracy of the subsequent solutions (Step II).

2. Model implementation and solution strategy

All the 3D Vickers indentation geometry models are carried out in displacement control mode using the static analysis and the parametric solver of the Structural Mechanics Module of Comsol Multiphysics 3.5a [11,12,13]. This choice is imposed to overcome the incapability of the current version of Comsol to solve time dependent elastoplastically promoted contact problems with friction. We refer to this kind of solution method to as pseudo-transient solution as the user defined displacement parameter works as a pseudo-time dependent parameter. The final solution is searched iteratively by a multistage sequence of static elastoplastic solutions, under the control of the varying displacement parameter. At each stage, the geometric configuration in current stage is calculated by using that from the previous stage. The damped Newton method is used to solve each stage. The direct UMFPACK is used to solve the algebraic linear system.
The whole indentation loading history is split into two loading regions, namely, the loading and the unloading part. In the case of the unloading part, the assigned increments for the displacement parameter are set smaller, i.e., 0.0005 vs 0.001 of the unloading part.

2.1.3 The contact problem

In Comsol Multiphysics the contact problems are solved by defining an initial contact pair consisting of a master and a slave [14,15]. In the present case the indenter is assumed to be the master and the sample the slave.
The contact problem is solved by the *augmented Lagrangian* method. The contact pressure T_n and the friction tractions T_{tx} and T_{ty} are the augmented variables and the *lumped solver* (with 25 as maximum number of iterations) is chosen.
The gap distance (*g)* between the slave and the master boundaries is computed to determine the value of the normal contact pressure and the value of the components of the friction traction vector [14]. The solver continually checks for the

current status of the gap elements until the force equilibrium is achieved within a specified tolerance value. For the augmented Lagrangian components, this value is se to 0.1 MPa, in order to ensure a non intrusive contact between the indenter and the sample disk.
An initial contact pressure and an initial friction force (i.e. 10^{-3} MPa along the z-direction and 10^{-3} MPa along x, y and z-direction) are imposed in order to constrain both the indenter and the sample and to prevent the solvers' failure. This results in a very small deformation in the initial contact configuration. The direct search method is selected.
The cohesion sliding resistance (*cohe*), the maximum friction traction (T_{tmax}) and the static friction coefficient (μ) are set to 0 MPa, infinite and 0.66 respectively [16].
A manual scaling of 0.01, for the *x*, *y* and *z*-displacements, and of 10 for both the contact pressure and the friction tractions is imposed. The relative tolerance is set to 10^{-4}.
The Rayleigh damping parameters, α_{dM} and β_{dK}, are set to 1 s^{-1} and 0,001 s respectively for both the indenter and the sample.

2.1 Bulk

A fully bulk mechanical behavior is assumed for the sample disk, i.e. the scale length of the depth of penetration is higher than the characteristic microstructural grain size of the alloy.

a)

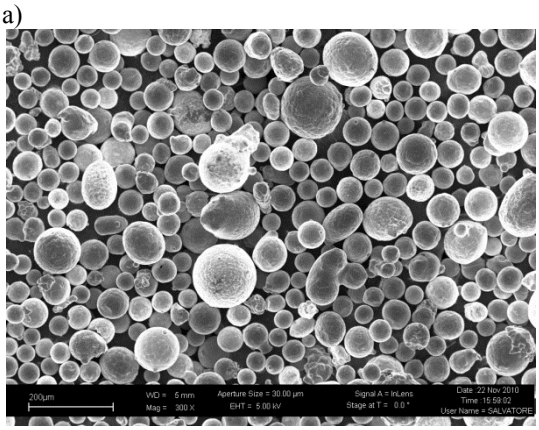

b)

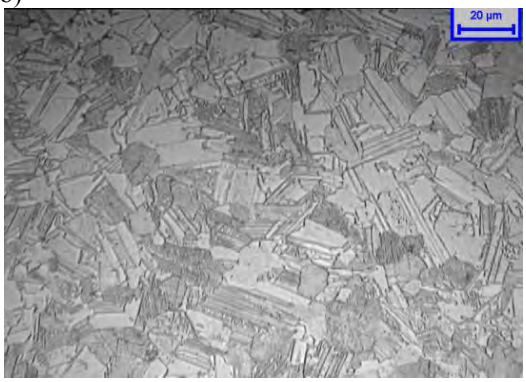

c)

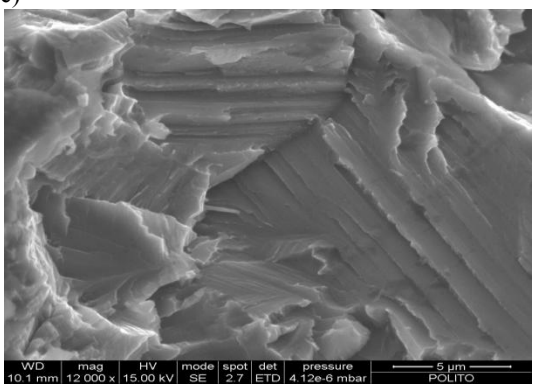

Figure 10. a) FESEM image (300 X) of the initial morphology of the prealloyed powders used as starting materials in the EBM chamber. Mean particle size: 150 µm. b) Optical microstructure of TiAl alloy after HIP at 1260°C for 4h at 1700 bar and heat treatment (500 X). Larger microstructural features are 30 µm. c) SEM cleavage fracture surface analysis (12000 X): duplex microstructure is still recognizable in the lamellar zones.

The required materials properties of the sample disk are taken from an experimental true stress - true strain curve.
Uniaxial tensile tests were performed at room temperature using a MTS servohydraulic machine operated at 0.1 mm/min. Tensile test's specimen are round being machined from hipped EBM processed rods, then turned with a gage length of 25 mm and gage diameter of 5 mm and finally screwed. From the true flow curve, the elastic modulus of 170 GPa, the offset yield stress of 450 MPa and the isotropic tangent modulus of 15.500 GPa are derived. The Poisson ratio is set to 0.263.

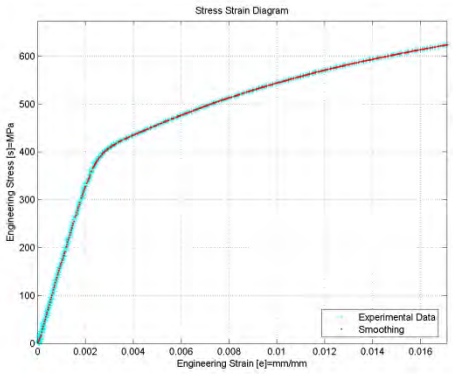

Figure 11. Experimental uniaxial true stress-true strain tensile curve; a smoothing curve is superimposed.

All these values are in accordance with the literature [3,4] and are peculiar of the duplex microstructure (consisting of γ grains and α_2/γ lamellar regions).
The static friction coefficient is set to 0.66 in accordance to literature data [16].
The Vickers indenter is considered isotropic and characterized by a Young's modulus of 1141 GPa and a Poisson's ratio of 0.100 [8,9].
Experimental instrumented indentation test are conducted using a prototype indentation machine specially designed in order to operate in the macro force range (i.e. loads larger than 2 N):

Figure 12. Universal Hardness Testing Machine OMAG SR-HU 09 produced by Omag Affri S.p.a.

3. Results and Discussion

The calculated ICs are drawn in terms of the total reaction force along the z direction versus the z displacement of the apex point of the indenter. Figure 13 shows experimental ICs and calculated ICs in the case of the ideal Vickers tip.

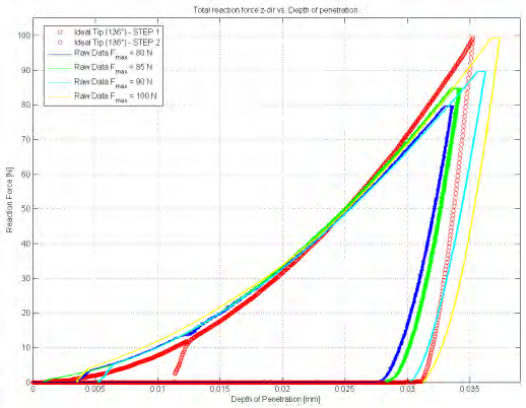

Figure 13. Calculated indentation curves (red – Step I and Step II – respectively F_{max_I}=11.7N, h_{max_I}=12.5μm and F_{max_II}=99.2N, h_{max_II}=35.2μm) vs experimental indentation curves (blue – F_{max}=80N and h_{max}=33.5μm, green – F_{max}=85N and h_{max}=34.3μm, cyan – F_{max}=90N and h_{max}=36.3μm, – yellow F_{max}=100N and h_{max}=37.4μm).

The calculated indentation curves show a good agreement when compared with their experimental counterparts. A prior validation test against experiments is assessed by overlapping the loading curves. The red calculated curve is then compared with four experimental curves each of which corresponds to a different maximum force value. A second validation test is made by comparing the slopes of the unloading curves. Here the offset is more appreciable and this is probably due to the constitutive law that assumes an isotropic hardening behaviour. Moreover, a significantly decrease in the number of the detected contact points is recorded during the unloading. This suggests that a denser mesh has to be used before reaching the maximum load up to the end of the unloading part of the whole indentation cycle.
The following figure shows all the calculated indentation curves:
Figure 14 clearly indicates how different tip geometries can lead to different indentation curves. In particular, blunted or truncated indenters require higher loads to penetrate into the sample disk.
In the case of ideal Vickers tips with difference in the apex angle of only 0.4° it is possible to record a different trend for higher loads.
In the case of experimental indentation curves the zero point must be evaluated by linear regression analysis [8] due to difficulties in

recording very small loads and to the unknown actual geometry of the tip of the indenter.

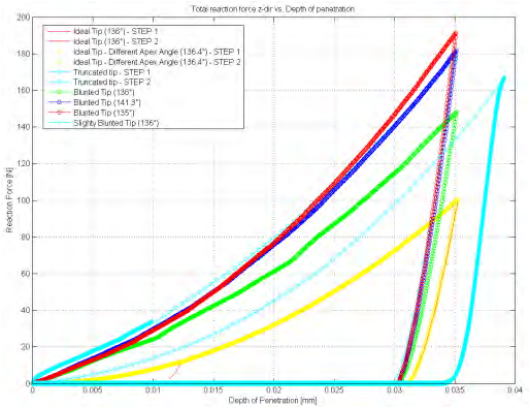

Figure 14. Calculated indentation curves:
► Red – Ideal tip 136° Step I and Step II - respectively F_{max_I}=11.7N, h_{max_I}=12.5µm and F_{max_II}=99.2N, h_{max_II}=35.2µm;
► Yellow points – Ideal tip with apex angle of 136.4° Step I and Step II – F_{max}=100.6N and h_{max}=35.2µm;
► Cyan points – Truncated tip Step I ad Step II – F_{max}=179.4N and h_{max}=35.1µm;
► Green points – Blunted 136° tip – F_{max}=148.2N and h_{max}=35.1µm;
► Blue points - Blunted 141.3° tip – F_{max}=181.7N and h_{max}=35.1µm,
► Red points – Blunted 135° tip – F_{max}=191N and h_{max}=35.1µm;
► Cyan squares – Slightly blunted 136° tip – F_{max}=166.8N and h_{max}=39.1µm.
Note that the results for Ideal tip 136° (Step I and Step II) overlaps the calculated curve for Ideal tip with apex angle of 136.4° and hence may appear to be yellow.

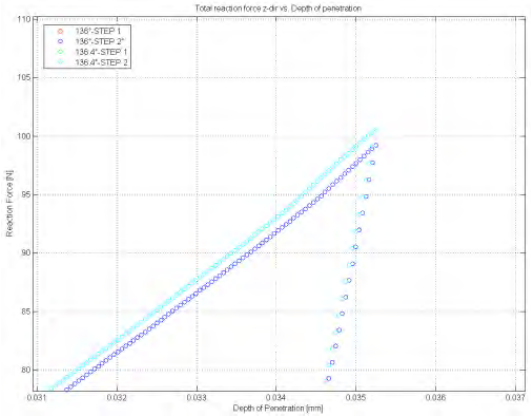

Figure 15. Comparison of the calculated indentation curves near the maximum load in the case of ideal tip 136° Step II (blue - F_{max_II}=99.2N and h_{max_II}=35.2µm) and ideal tip with apex angle of 136.4° Step II (cyan - F_{max}=100.6N and h_{max}=35.2µm).

Nevertheless, the zero point can be directly estimated by the calculated curve without resorting to the interpolation of the experimental raw data.

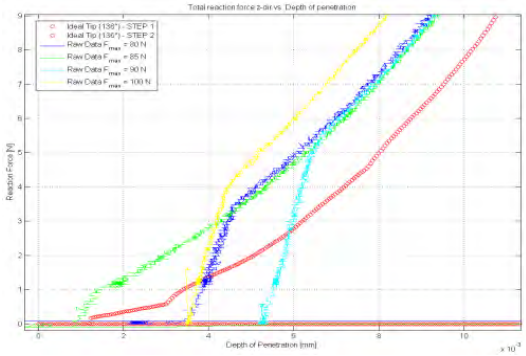

Figure 16. Zero-point region in the case of the calculated ideal Vickers tip (red) and of the experimental ICs already shown in figure 13.

The calculated curves in the zero- point region are shown in the following figure.
The truncated tip has the largest curvature in the initial contact point. Owing to the involved larger initial contact area, a larger load has to be initially applied in order to induce a specified displacement of the indenter.

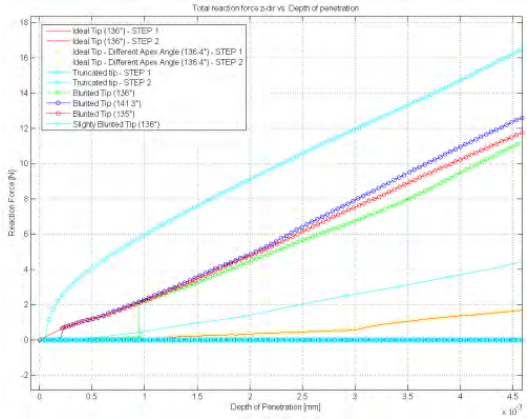

Figure 17. Zero point zone in the case of the calculated experimental ICs already shown in figure 14.

The calculated loads in the other tip geometries are lower due to the higher localized pressure induce by sharper tips. Only in the case of the ideal tip of 136° and 136.4°, the same trend is

found at the beginning, thereby proving that the influence of the apex angle on the ideal indenter is negligible for low loads.
Figure 18 shows an unexpected behavior of the indenter. Even it is perfectly rigid, it elastically deforms during the incipient contact by originating a curved surface.

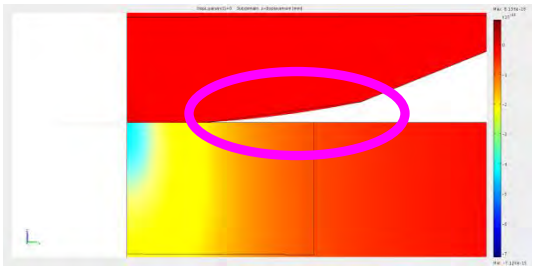

Figure 18. The pink circle indicates the deformation of the tilted planes in the initial stage of contact for blunted indenters.

In figure 19 a decease in the surface area of the sample is noticed during the indentation cycle far from the indenter's diagonals (see). This behavior has to be taken in account for reliable hardness measurement based on the evaluation of the real contact area.
This phenomena is also reported in the literature [10] and is recorded during experiments. It consists in the formation of a residual concave impression which suggests that the exponent in Oliver and Pharr fitting equation is not 2 as predicted by the elastic theory but ranges between 1.2 and 1.6 [10].

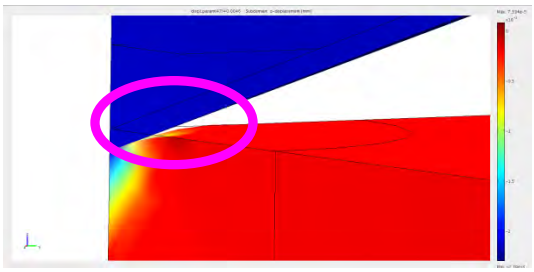

Figure 19. Lowering of the surface of the sample is indicated in the pink circle.

The calculated residual imprint is shown in figure 20. It can be considered as the input data for traditional hardness measurements.

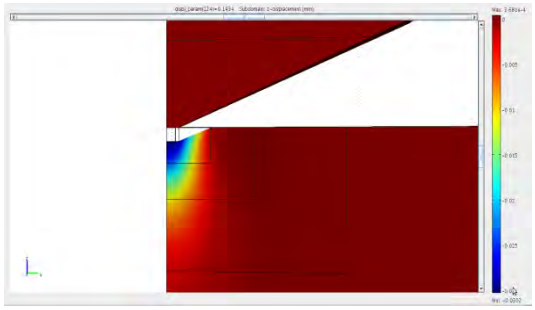

Figure 20. z-displacement associated to the residual imprint for a truncated tip.

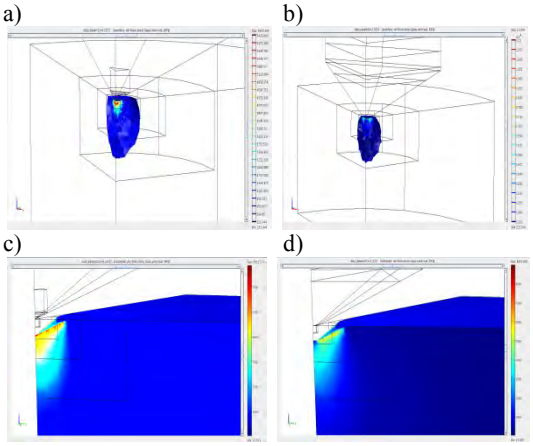

Figure 21. Effective von Mises stress distribution for the initial contact (Step I) and for the maximum depth of penetration (h_{max}=35.1μm) . a) and c) refer to ideal tip, b) and d) to truncated tip. Von Mises max value are: Perfect tip: 6851 MPa – Truncated tip: 8977 MPa.

Figure 21 shows that the stress field is highly localized initially around the indenter tip and that, for larger depths of penetration the involved deformed region progressively extend inside the disk. The deformed geometry does not show up any pile-up, but only sink-in. This is due to the large hardness of the TiAl alloy as experimentally proved [17]. The larger value of the von Mises stress is achieved near the maximum value of the imposed displacement and it is lower for sharper indenter. Von Mises stress is highly localized near the diagonals of the indenter for all the modeled geometries.
The x-, y- and z-displacements are shown in figure 22.
The progress of the contact area during indentation can be best estimated by inspecting the contact pressure along the slave boundary arc length for various displacement parameters.

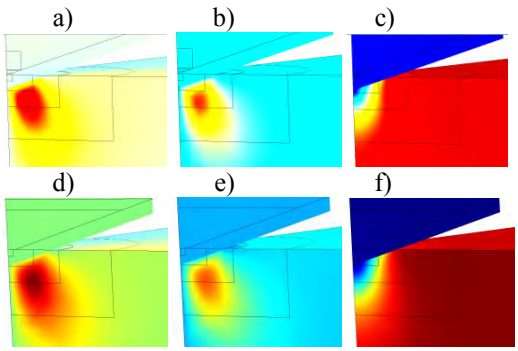

Figure 22. a) and d) x-displacements (max value: Perfect tip: $4.616 \cdot 10^{-3}$ mm – Truncated tip: $5.515 \cdot 10^{-3}$ mm); b) and e) y displacements (max value: Perfect tip: $5.830 \cdot 10^{-3}$ mm – Truncated tip: $7.699 \cdot 10^{-3}$ mm), c) and f) z displacements (max value: Perfect tip: 0.0667 mm – Truncated tip: 0.0667 mm).

The maximum achieved displacement parameter is equal to h_{max}=35.1µm for both the ideal and the truncated tips.

a)

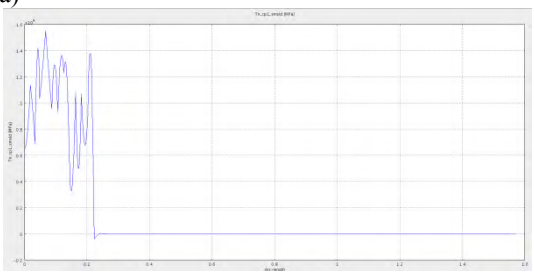

The first null contact pressure points are located at 0.222 and 0.272 mm arc-lengths for the ideal

b)

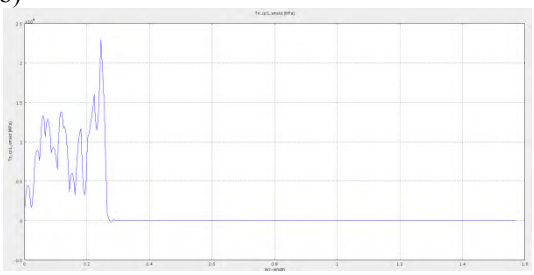

Figure 23. Contact pressure progress vs slave boundary arc length for h_{max}=35.2µm. a) Ideal tip; b) Truncated tip.

and the truncated tip geometry respectively. Assuming an ideal (i.e. rigid) indenter and the extension of the calculated sink-in [17] at the maximum contact depth of 35.1 µm, a contact area of 0.00819 and 0.01272 mm^2 can be estimated for the ideal and the truncated tips respectively. These values correspond to a contact area of 0.0302 and 0.0555 mm^2 for the ideal and the truncated tips respectively. Based on these estimated contact areas, the estimated indentation hardness may range from 3285 MPa for ideal tip to 3232 MPa for a truncated tip.

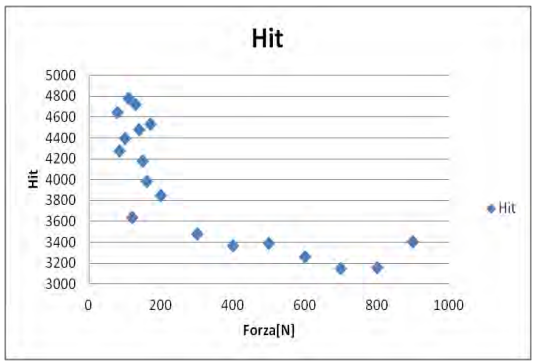

Figure 24. Experimental indentation hardness (Hit) evaluated by means of OMAG SR-HU 09 machine. At low load (F < 300 N), the used indentation machine prototype is not capable to record a constant value of Hit due to the large uncertainty associated with lower loads.

Thus, as shown in figure 24, the developed 3D Vickers model suggests that the indentation hardness values measured with the given indentation machine are not accurate for low loads. Indeed, the calculated indentation hardness can be used to correct the experimental values when these are affected by large uncertanties.

7. Conclusions

Computationally, the 3D Vickers indentation problem is strongly non linear, involves large displacements and strong singularities at the indenter tip. Three basic factors have to be taken into account to accurately describe the indentation contact problem: a) friction, b) tip geometry and c) material. The developed 3D Vickers model is applied to estimate the materials proprieties of γ-TiAl based on macro-indentation tests. In addition, the model allows to: 1) understand whether the experimental tests

can fulfill current constitutive laws (unless some adjusting parameters) and how to eventually improve them; 2) evaluate the relative importance of the tip geometry and of friction effect; 3) evaluate the stress field state inside the specimen and 4) the minimum geometry of the disk sample for correct bulk mechanical properties; 5) refining the input parameters of Oliver and Pharr's method; 6) predict sink-in phenomena; 7) eventually correct experimental values of the indentation hardness. Finally, the zero-point correction and the value of the contact area depend on the tip geometry and can be effectively predicted by the developed model.

8. References

1. D.M. Dimiduk, Gamma titanium aluminide alloys – an assessment with the competition of aerospace structural materials, *Mater. Sci. Eng.ng*, **A263**, 281-288 (1999).
2. X. Wu, Review of alloy and process development of TiAl alloys, *Intermetallics*, **14**, 1114-1122 (2006).
3. Z.H. Huang, Workability and microstructure evolution of Ti–47Al–2Cr–1Nb alloy during isothermal deformation, *Intermetallics,* **13**, 245–250 (2005).
4. M. Thomas, O. Berteaux, F. Popoff, M. Jouiad, G. Hénaff, Microstructure dependence of the strain hardening rate in a PM Ti-48Al-2Cr-2Nb alloy, *3rd International Workshop on γ-TiAl Technologies, Bamberg*, **6.7**, (2006).
5. J.L. Hay, G.M. Pharr, *Instrumented Indentation Testing*, ASM handbook nano-indentation, (1994).
6. S. Takagi, K. Kamijo, T. Usuda, H. Kawachi, K. Hanaki, *Wide-range verification of the geometry of Vickers diamond indenters*, XVIII Imeko World Congress, Metrology for a Sustainable Development, September, 17–22, Rio de Janeiro, Brazil (2006).
7. W.C. Oliver, G.M. Pharr, *An improved technique for determining hardness and elastic modulus using load and displacement sensing indentation experiments*, J. Mater. Res., 7(6) 1564-1583 (1992).
8. UNI EN ISO 14577-1, *Materiali metallici – Prova di penetrazione strumentata per la determinazione della durezza ed altri parametri dei materiali* – Parte 1: Metodo di prova, dicembre (2004).
9. UNI EN ISO 14577-2, *Materiali metallici – Prova di penetrazione strumentata per la determinazione della durezza ed altri parametri dei materiali* – Parte 2: Verifica e taratura delle macchine di prova, dicembre (2004).
10. A.C. Fisher-Cripps, *Nanoindentation*, Springer-Verlag, New York, (2002).
11. Loc Vu-Quoc, Xiang Zhang, An elastoplastic contact force–displacement model in the normal direction: displacement-driven version, *Proc. R. Soc. Lond.* A455, 4013–4044 (1999).
12. Comsol Multiphysics, *Structural Mechanics Module*, User's Guide, Vers. 3.5, (2008).
13. Comsol Multiphysics, *Structural Mechanics Module*, Model Library, Vers. 3.5, (2008).
14. Comsol Multiphysics, *Structural Mechanics Module*, Reference Guide, Vers. 3.5, (2008).
15. J.C. Simo, T.A. Laursen, *An augmented lagrangian treatment of contact problems involving friction*, Comp. & Struct., 42(1), 97-116, (1992).
16. C.L. Chu, S.K. Wu, *A study on the dry uni-directional sliding behaviour of titanium aluminides*, Scripta Metall. et Mater., 33(1) 139-143, (1995).
17. R. Cagliero, G. Maizza, Modeling of Vickers Indentation of TiAl Alloys, Excerpt from the Proceedings of the COMSOL Conference, Paris, (2010).

8. Acknowledgements

The authors wish to express their sincere appreciation to Regione Piemonte (local government) – Direzione Regionale alle Attività Produttive - for funding the Green Engine for Air Traffic 2020 (Great 2020 - Ecoprolab) research project of Bando Regionale 24/12/2007 – Misura Ri.7 – Asse 1 "Ricerca e Innovazione" – (LR 34/2004) for supporting the present research work. Also, AVIO S.P.A. group (Rivalta – TO), the AVIOPROP s.r.l. (NO) and OMAG-AFFRI of Induno Olona (VA) are deeply acknowledged.